# Chronophin Dimerization Is Required for Proper Positioning of Its Substrate Specificity Loop[*][S]

**Christian Kestler**[‡1,2], **Gunnar Knobloch**[‡§1], **Ingrid Tessmer**[§], **Elisabeth Jeanclos**[‡], **Hermann Schindelin**[§], and **Antje Gohla**[‡§3]

From the [‡]Institute for Pharmacology and Toxicology, University of Würzburg, 97078 Würzburg, Germany and [§]Rudolf Virchow Center for Experimental Biomedicine, University of Würzburg, 97080 Würzburg, Germany

**Background:** The role of homodimerization in the family of C2a-capped HAD phosphatases is unknown.
**Results:** Chronophin homodimerization is required for proper positioning of the substrate specificity loop and for substrate dephosphorylation.
**Conclusion:** The specificity of chronophin is allosterically controlled by a homophilic intermolecular interaction.
**Significance:** Our results reveal a general principle of how HAD hydrolase dimerization can contribute to substrate specificity.

Mammalian phosphatases of the haloacid dehalogenase (HAD) superfamily have emerged as important regulators of physiology and disease. Many of these enzymes are stable homodimers; however, the role of their dimerization is largely unknown. Here, we explore the function of the obligatory homodimerization of chronophin, a mammalian HAD phosphatase known to dephosphorylate pyridoxal 5′-phosphate (PLP) and serine/threonine-phosphorylated proteins. The exchange of two residues in the murine chronophin homodimerization interface (chronophin[A194K,A195K]) yields a constitutive monomer both *in vitro* and in cells. The catalytic activity of monomeric chronophin toward PLP is strongly impaired. X-ray crystallographic studies of chronophin[A194K,A195K] revealed that dimer formation is essential for an intermolecular arginine-arginine-tryptophan stacking interaction that positions a critical histidine residue in the substrate specificity loop of chronophin for PLP coordination. Analysis of all available crystal structures of HAD hydrolases that are grouped together with chronophin in the C2a-type structural subfamily uncovered a highly conserved mode of dimerization that results in intermolecular contacts involving the substrate specificity loop. Our results explain how the dimerization of HAD hydrolases contributes to their catalytic efficiency and substrate specificity.

Enzymes of the haloacid dehalogenase (HAD)[4]-type constitute a large and ancient superfamily whose members are pres-

ent in all three kingdoms of life. The majority of HAD enzymes are phosphatases known to cover an exceptionally broad substrate space, ranging from metabolites to macromolecules such as DNA and serine/threonine (Ser/Thr)- or tyrosine (Tyr)-phosphorylated proteins (1–3). A number of HAD phosphatases have been causally linked to human diseases, including cancer and cardiovascular, metabolic, and neurological disorders (4); however, very little is currently known about the regulation of these enzymes.

Contrasting their structurally highly diverse substrates, HAD phosphatases are remarkably similar in terms of topology and active site architecture even though their overall amino acid sequence identities are very low (3). A canonical, modified Rossmann fold positions the catalytic core residues that are distributed over four HAD motifs. The first aspartate in the strictly conserved D$X$D$X$(V/T) HAD phosphatase signature motif serves as the nucleophile and phosphoryl group acceptor that forms a phosphoaspartate intermediate during catalysis. This aspartate also coordinates the catalytically essential Mg$^{2+}$ ion (1).

HAD phosphatases are additionally equipped with so-called cap domains. Unlike the structurally stereotypical buildup of the catalytic domain, caps are highly diversified modules that can be grouped into four classes, C0, C1, C2a, or C2b, according to their size, structure, and insertion site in the core domain (3). A primary cap function is to mediate solvent occlusion/inclusion during the catalytic cycle. In general, C1/C2-capped HAD phosphatases process small metabolites that can be sequestered within the active site by cap closure, thus ensuring efficient dephosphorylation. In contrast, macromolecules themselves can provide the necessary active site shielding and are preferentially processed by C0 ("capless") phosphatases. Besides contributing to catalytic efficiency, caps supply substrate specificity determinants with residues that engage in substrate recognition and thereby establish phosphatase specificity (5–8). Interestingly, caps can also mediate the commonly found HAD phosphatase oligomerization: among the 20 structurally characterized human HAD phosphatases alone, 10 are oligomeric, and in four of these phosphatases, oligomerization is mediated by cap-cap interactions (4).

Chronophin is a homodimeric, C2a-capped HAD phosphatase (9–11) known to target Ser[3]-phosphocofilin (12–16) and the Ser/Thr-phosphorylated steroid receptor co-activators 1 and 3 (17). In addition to its emerging protein phosphatase activities, chronophin (gene name, pyridoxal phosphatase (*PDXP*)) acts as a small molecule phosphatase dedicated to the metabolism of pyridoxal 5′-phosphate (PLP) (10, 11). PLP is the biologically active form of vitamin $B_6$ that functions as a cofactor in the catalysis of >160 different enzymatic reactions, in particular in the biosynthesis of neurotransmitters (18, 19). Chronophin has been suggested to link pathological alterations in vitamin $B_6$ metabolism with cofilin-dependent actin dynamics in the rat hippocampus following status epilepticus (20, 21).

In the present study, we show that chronophin homo-dimerization is a prerequisite for its proper enzymatic function as a PLP phosphatase. These findings can be extended to dimeric C2a-capped HAD hydrolases in general and indicate a paradigmatic role for their dimerization in substrate recognition and thus in the control of catalytic efficiency and substrate specificity.

## EXPERIMENTAL PROCEDURES

*Database Searches*—The Protein Data Bank was searched for structures of haloacid dehalogenase-like hydrolases using the Pfam entries PF13419, PF00702, PF13344, PF13242, PF08282, and PF12710. The search was conducted with a 90% sequence identity cutoff to reduce the number of multiple entries and mutant proteins and yielded 177 unique entries. Cap domain subtypes were determined manually and cross-validated using a recently published data set (22). The PISA online tool (23) was used to determine the oligomeric state and for dimer interface calculations (see supplemental Table S1).

*DNA Constructs*—Murine chronophin cDNA was reverse transcribed from adult mouse brain tissue. Total RNA was isolated using TRIzol (Invitrogen) according to the manufacturer's instructions, and cDNA was obtained with the High Fidelity RNA PCR kit (Takara Bio Inc.) and oligo(dT) primers. The PCR product was subcloned into the BamHI and EcoRI restriction sites of pcDNA3 (Invitrogen) to construct untagged chronophin, into the KpnI and XhoI sites of pENTR3C (Invitrogen) followed by insertion via homologous recombination into pDEST27 (Invitrogen) to produce GST-tagged chronophin for expression in mammalian cells, or into the bacterial expression vector pETM11 (European Molecular Biology Laboratory) to create N-terminally His$_6$-tagged chronophin for *in vitro* studies. The chronophin[A194K,A195K] (chronophin[KK]) construct was generated by site-directed mutagenesis.

*Protein Expression and Purification*—His$_6$-tagged chronophin wild type or chronophin[KK] in pETM11 was transformed into BL21(DE3) cells (Stratagene) and expressed for 18 h at 20 °C after induction with 0.5 mM isopropyl β-D-1-thiogalactopyranoside. To increase solubility, chronophin was co-expressed with chaperones from the pG-Tf2 plasmid (Takara Bio Inc.) according to the instructions of the manufacturer. Cells were harvested at 8,000 × g for 10 min and lysed in 100 mM triethanolamine (TEA), 500 mM NaCl, 20 mM imidazole, 5 mM MgCl$_2$, pH 7.4 in the presence of protease inhibitors (EDTA-free protease inhibitor tablets, Roche Applied Science)

and 150 units/ml DNase I (Applichem) using a cell disruptor (Microfluidizer Processor M-110 P, Microfluidics). Cell debris was removed by centrifugation for 30 min at 30,000 × g. For purification, cleared supernatants were loaded on a HisTrap HP column operated on an ÄKTA liquid chromatography system (GE Healthcare) in binding buffer (50 mM TEA, 500 mM NaCl, 20 mM imidazole, 5 mM MgCl$_2$, pH 7.4), and His$_6$-tagged proteins were eluted using a linear gradient up to 50% elution buffer (50 mM TEA, 250 mM NaCl, 500 mM imidazole, 5 mM MgCl$_2$, pH 7.4). Fractions containing His$_6$-tagged chronophin were pooled, and the His$_6$ tag was cleaved with tobacco etch virus protease for 2 days at 4 °C. Subsequently, cleaved protein was separated from uncleaved protein and from the His$_6$-tagged tobacco etch virus protease on a HisTrap HP column. Untagged chronophin was further purified on a HiLoad 16/60 Superdex 200 prep grade size exclusion chromatography column (GE Healthcare) in buffer A (50 mM TEA, 250 mM NaCl, 5 mM MgCl$_2$, 5% (v/v) glycerol, pH 7.4).

*Analytical Size Exclusion Chromatography*—Globular proteins of known molecular weight (Gel Filtration LMW Calibration kit, GE Healthcare) were used to calibrate a Superdex 200 10/300 GL column (GE Healthcare), and blue dextran was used to determine the column void volume. Protein elution volumes were measured by monitoring the absorption at 280 nm. The elution volumes were used to calculate the partition coefficient ($K_{av}$) with the formula $K_{av} = (V_e - V_0)/(V_t - V_0)$ where $V_e$ is the elution volume, $V_0$ is the void volume, and $V_t$ is the total volume of the column. The apparent molecular weight was then derived from the inverse logarithm of the partition coefficient.

*Analytical Ultracentrifugation*—Sedimentation velocity analytical ultracentrifugation was carried out using a Beckman Optima XL-I analytical ultracentrifuge (Beckman Coulter) with an eight-hole An-50 Ti rotor at 40,000 rpm at 20 °C. Four hundred microliters of dialyzed, purified recombinant protein dialyzed against buffer A without glycerol and reference buffer solution were loaded in standard double-sector charcoal-filled Epon centerpieces equipped with sapphire windows. Protein concentration corresponded to an $A_{280}$ of 0.5–0.8. Data were collected in continuous mode at a step size of 0.003 cm using absorption optical detection at a wavelength of 280 nm. Data were analyzed using the NIH software SEDFIT to determine continuous distributions for solutions to the Lamm equation *c*(*s*) as described previously (24). Analysis was performed with regularization at confidence levels of 0.68 and floating frictional ratio ($f/f_0 \sim 1.32 \pm 0.02$ for both chronophin wild type and mutant, suggesting a globular conformation), time-independent noise, baseline, and meniscus position to root mean square deviation (r.m.s.d.) values between 0.007 and 0.012. Consistent results were obtained in three independent experiments.

*Atomic Force Microscopy (AFM)*—Proteins were diluted between 30- and 100-fold from 30 μM stock solutions in AFM deposition buffer (25 mM HEPES, 50 mM KCl, 10 mM MgCl$_2$, pH 7.5), immediately deposited onto freshly cleaved mica, rinsed with deionized water, and dried in a gentle stream of nitrogen. All images were collected on an MFP-3D-BIO atomic force microscope (Asylum Research) in oscillating mode using Olympus OMCL-AC240 silicon probes with spring constants of ~2 newtons/m and resonance frequencies of ~70 kHz.

Images were captured using Asylum Research software on Igor Pro at a scan size of $2 \times 2 \ \mu m^2$, a scan rate of 0.5 Hz, and a resolution of $1024 \times 1024$ pixels. For analysis, AFM images were flattened to third order. AFM volumes were measured using the NIH Image-based software ImageSXM and used to calculate protein molecular weights as described (25) with the formula $V = 1.2 \times (MW) - 5.9$ where $V$ is the AFM volume and MW is the molecular weight. Molecular weights (and error ranges) were derived from the center positions (and two standard deviations) of Gaussian fits with $R^2 > 0.79$ or 0.96 for chronophin$^{WT}$ or chronophin$^{KK}$, respectively) to the distributions of measured volumes using the software Origin (Origin-Lab, version 8.6). Consistent results were obtained from triplicate experiments for both chronophin$^{WT}$ and chronophin$^{KK}$.

*Isothermal Titration Calorimetry (ITC)*—ITC experiments were performed on a MicroCal ITC$_{200}$ microcalorimeter (GE Healthcare) at 25 °C and were analyzed using MicroCal Origin software. Prior to all ITC experiments, protein samples were extensively dialyzed overnight at 4 °C against filtered and degassed buffer A. Each titration experiment consisted of $2.5-\mu l$ injections of $300-600 \ \mu M \ BeF_3^-$ diluted in buffer A into the $280-\mu l$ sample cell containing $25-75 \ \mu M$ chronophin. Heats of dilution measurements were carried out as mentioned above by injecting $BeF_3^-$ into buffer A. For each experiment, the binding enthalpy was directly measured, whereas the stoichiometry ($N$) and the dissociation constant ($K_d$) were obtained using the analysis software, assuming a single site binding model.

*Crystallization and Data Collection*—Proteins were concentrated to $8-10$ mg/ml (as determined by absorption at 280 nm using a calculated molar extinction coefficient of 18,450 $M^{-1} \cdot cm^{-1}$) in buffer A (chronophin$^{KK}$) or in 10 mM TEA, 100 mM NaCl, 1 mM MgCl$_2$ (chronophin$^{WT}$) using 10,000 molecular weight cutoff centrifugal filter devices (Amicon Ultra-15, Millipore). All crystals were grown at 20 °C using the hanging drop vapor diffusion method by mixing equal volumes of protein solution with reservoir solution. Chronophin$^{KK}$ crystals were grown in 0.1 M MES at pH 6.5 with 25% (w/v) polyethylene glycol monomethyl ether 550 and appeared as thin plates after $3-4$ days. Chronophin$^{WT}$ was crystallized in 0.1 M imidazole, 0.2 M NaCl, 1 M sodium tartrate supplemented with 1 mM $BeF_3^-$ to obtain the chronophin$^{WT}$-$BeF_3^-$ structure, and cubic crystals appeared within 24 h. All crystals were cryoprotected for flash cooling in liquid nitrogen by soaking in mother liquor containing 30% (v/v) glycerol. All data sets were collected at beamline 14.1 (Berliner Elektronenspeicherring-Gesellschaft für Synchrotronstrahlung (BESSY), Berlin, Germany). Data were processed using iMOSFLM (26) and Scala from the CCP4 program suite (27). All three structures were solved by molecular replacement with the program Phaser (28) using human pyridoxal 5′-phosphate phosphatase/chronophin (Protein Data Bank code 2OYC) as a search model. The chronophin$^{WT}$/chronophin$^{WT}$-$BeF_3^-$ structures were refined at 2.2-Å resolution, and the chronophin$^{KK}$ structure was refined at 1.75-Å resolution with Phenix (29), incorporating torsion angle *non-crystallographic symmetry* restraints. Structural representations were generated with PyMOL (The PyMOL Molecular Graphics System, version 1.5.0.4, Schrödinger, LLC). PyMOL was also used to determine the r.m.s.d. of structural alignments.

*In Vitro Phosphatase Assays*—PLP dephosphorylation assays were conducted in 96-well microtiter plates. Chronophin$^{WT}$ or chronophin$^{KK}$ (100 nM/well) was preincubated for 10 min at 22 °C in buffer A supplemented with 0.001% (v/v) Triton X-100. The reactions were started by the addition of PLP (final concentrations ranging from 0 to 1,000 $\mu M$ in a total volume of 50 $\mu l$) and stopped after 2 min by the addition of 100 $\mu l$ of Biomol Green (Enzo Life Sciences). Color was allowed to develop for 10 min before the absorbance of the resulting phosphomolybdate complex was read at 620 nm on an Envision 2104 multilabel microplate reader (PerkinElmer Life Sciences). Free phosphate release was quantified using phosphate standard curves, and $V_{max}$ and $K_m$ values were calculated using GraphPad Prism version 6 (GraphPad Software Inc.). The lines were fitted by nonlinear regression using the least square fitting method.

*Cell Transfection and Pulldown Assays*—HEK293-AD cells (Stratagene) were cultured in Dulbecco's modified Eagle's medium (DMEM) containing 10% (v/v) fetal calf serum (FCS), 2 mM L-glutamine, 100 units/ml penicillin, and 100 $\mu g$/ml streptomycin. Cells were plated at a density of $4.5 \times 10^5$ cells in 6-well plates and transfected the next day using TransIT-LT1 (Mirus) with a total amount of 1 $\mu g$ of DNA. The amount of transfected DNA was kept constant with empty vector. Cells were lysed in 50 mM TEA, 250 mM NaCl, 5 mM MgCl$_2$, 1% (v/v) Triton X-100, 10 $\mu g$/ml leupeptin, 10 $\mu g$/ml pepstatin A, 50 $\mu g$/ml aprotinin, 1 mM 4-(2-aminoethyl)benzenesulfonyl fluoride (Pefabloc) for 15 min at 4 °C under constant rotation. After centrifugation at $15,000 \times g$ for 15 min at 4 °C, the lysates were incubated for 1.5 h under constant rotation with glutathione-Sepharose 4B beads (GE Healthcare) pre-equilibrated with washing buffer (50 mM TEA, 250 mM NaCl, 5 mM MgCl$_2$, 1% (v/v) Triton X-100). The beads were washed four times with washing buffer using a vacuum manifold, bead-associated proteins were eluted with Laemmli sample buffer, and eluates were separated by SDS-PAGE and blotted onto nitrocellulose membranes (Hybond C, Amersham Biosciences). Chronophin dimerization was assessed by Western blot analysis with chronophin-specific antibodies (clone C85E3, Cell Signaling Technology).

*Accession Codes*—The x-ray crystal structures of murine chronophin$^{WT}$ and murine chronophin$^{KK}$ have been deposited in the Protein Data Bank under accession codes 4BX3 (murine chronophin), 4BX2 (murine chronophin in complex with $BeF_3^-$), and 4BX0 (murine chronophin$^{A194K,A195K}$).

*Statistical Analysis*—Pulldown and ITC experiments were analyzed with the two-tailed unpaired $t$ test using GraphPad Prism version 6.

## RESULTS

*Homooligomer Formation Is a Common Feature of C2a-type HAD Hydrolases*—We analyzed a data set comprising all available HAD hydrolase structures from various species (see "Experimental Procedures" for details). Of the 177 unique entries, 104 HAD hydrolases (~59%) are likely to form homooligomers as compared with 72 structures that are assigned as monomers and with one heterooligomer. As shown in Table 1, C2a-type enzymes are particularly noteworthy because all available structures represent dimers (12 entries) or tetramers (five entries). However, the function of HAD hydrolase

**TABLE 1**

**Oligomeric states of structurally characterized HAD-type hydrolases**

The numbers of structures per structural subfamily and per oligomeric state are indicated. The corresponding Protein Data Bank entries and protein information can be found in supplemental Table S1.

| | Structural HAD subfamily | | | | | |
| | C0 | C1 | C1 + C2 | C2a | C2b | Structures/oligomeric state |
|---|---|---|---|---|---|---|
| Monomers | 11 | 40 | 6 | — | 15 | 72 |
| Dimers | 3 | 43 | 6 | 12 | 11 | 75 |
| Trimers | — | 2 | — | — | — | 2 |
| Tetramers | 10 | 4 | — | 5 | 1 | 20 |
| Hexamers | — | 1 | — | — | — | 1 |
| Octamers | 4 | 1 | — | — | — | 5 |
| Dodecamers | — | 1 | — | — | — | 1 |
| Heterodimers | — | 1 | — | — | — | 1 |
| Structures/subfamily | 28 | 93 | 12 | 17 | 27 | 177 |

**TABLE 2**

**Data collection and refinement statistics**

r.m.s., root mean square.

| | Chronophin$^{WT}$ | Chronophin$^{WT}$-BeF$_3^-$ | Chronophin$^{KK}$ |
|---|---|---|---|
| **Data collection** | | | |
| Wavelength (Å) | 0.91841 | 0.91841 | 0.91841 |
| Space group | I23 | I23 | P2 |
| Unit cell parameters | | | |
| $a$, $b$, $c$ (Å) | 167.10, 167.10, 167.10 | 166.83, 166.83, 166.83 | 36.13, 91.82, 39.19 |
| $\alpha$, $\beta$, $\gamma$ (°) | 90.00, 90.00, 90.00 | 90.00, 90.00, 90.00 | 90.00, 98.28, 90.00 |
| Resolution range (Å)[a] | 44.66–2.19 (2.31–2.19) | 44.59–2.19 (2.31–2.19) | 33.32–1.75 (1.84–1.75) |
| $R_{sym}$[b] | 0.082 (0.858) | 0.116 (1.12) | 0.093 (0.658) |
| $R_{p.i.m}$[c] | 0.034 (0.358) | 0.048 (0.472) | 0.049 (0.347) |
| $I/\sigma I$[d] | 12.9 (2.2) | 10.2 (1.8) | 10.2 (2.3) |
| Completeness (%) | 99.9 (99.7) | 100 (100) | 99.8 (99.9) |
| Multiplicity | 6.8 (6.7) | 6.7 (6.6) | 3.5 (3.5) |
| Total reflections | 269,875 | 266,023 | 89,076 |
| Unique reflections | 39,743 (5,736) | 39,582 (5,743) | 25,494 (3,709) |
| **Refinement** | | | |
| Wilson B-factor (Å$^2$) | 47.0 | 41.1 | 19.1 |
| Average B-factor (Å$^2$) | 48.4 | 45.5 | 28.6 |
| Macromolecules | 48.7 | 45.8 | 28.0 |
| Solvent | 40.6 | 39.2 | 34.2 |
| $R_{cryst}$[e] | 0.1707 | 0.1678 | 0.1913 |
| $R_{free}$[e] | 0.2067 | 0.2123 | 0.2363 |
| Number of non-hydrogen atoms | 4,645 | 4,676 | 2,496 |
| Macromolecules | 4,453 | 4,460 | 2,247 |
| Ligands | 14 | 28 | 7 |
| Water | 178 | 188 | 242 |
| r.m.s. deviations in | | | |
| Bond lengths (Å) | 0.015 | 0.014 | 0.005 |
| Bond angles (°) | 1.640 | 1.567 | 1.006 |
| Planar groups (Å) | 0.010 | 0.010 | 0.004 |
| Dihedral angles (°) | 15.91 | 15.31 | 13.14 |
| Coordinate error (Å)[f] | 0.25 | 0.27 | 0.28 |
| Ramachandran statistics[g] | | | |
| Favored (%) | 96.92 | 98.29 | 99.32 |
| Allowed (%) | 2.22 | 1.54 | 0.34 |
| Outliers (%) | 0.85 | 0.17 | 0.34 |
| MolProbity clashscore[h] | 9.83 | 11.83 | 11.63 |

[a] Numbers in parentheses refer to the respective highest resolution data shell in the data set.

[b] $R_{sym} = \Sigma_{hkl}\Sigma_i|I_i - I|/\Sigma_{hkl}\Sigma_i I_i$ where $I_i$ is the $i$th measurement, and $I$ is the weighted mean of all measurements of $I$.

[c] $R_{p.i.m.} = \Sigma_{hkl}(1/(n-1))^{1/2}\Sigma_i|I_i - I|/\Sigma_{hkl}\Sigma_i I_i$ where $n$ is the multiplicity of the observed reflection.

[d] Indicates the average of the intensity divided by its S.D. value.

[e] $R_{cryst} = \Sigma|F_o - F_c|/\Sigma|F_o|$ where $F_o$ and $F_c$ are the observed and calculated structure factor amplitudes. $R_{free}$, same as $R_{cryst}$ for 5% of the data randomly omitted from the refinement.

[f] Estimated coordinate error based on $R_{free}$.

[g] Ramachandran statistics indicate the fraction of residues in the favored, allowed, and disallowed regions of the Ramachandran diagram as defined by MolProbity (54).

[h] Number of serious clashes per 1,000 atoms (54).

dimerization is unclear as all catalytic core residues are encoded in a single polypeptide chain, and the available structures of oligomeric HAD hydrolases show that the adjacent protomer does not contribute active site residues. To understand the role of HAD dimerization, we investigated mammalian chronophin as a representative C2a-type family member.

*Crystallization and Structure Determination of Murine Chronophin*—We determined the three-dimensional structure of murine chronophin by x-ray crystallography and refined it by molecular replacement with human chronophin (Protein Data Bank code 2OYC and Ref. 9) to 2.2-Å resolution with an $R_{work}$ of 17.1% and an $R_{free}$ of 20.7% (Protein Data Bank code 4BX3). Data collection and refinement statistics are given in Table 2. The alignment of human and murine chronophin structures (Protein Data Bank codes 2OYC and 4BX3) shows an almost perfect superposition with a r.m.s.d. of 0.61 Å determined for the C$\alpha$ atoms of residues 1–290. Both orthologs crystallize as homodimers via the cap domain as shown for murine chro-
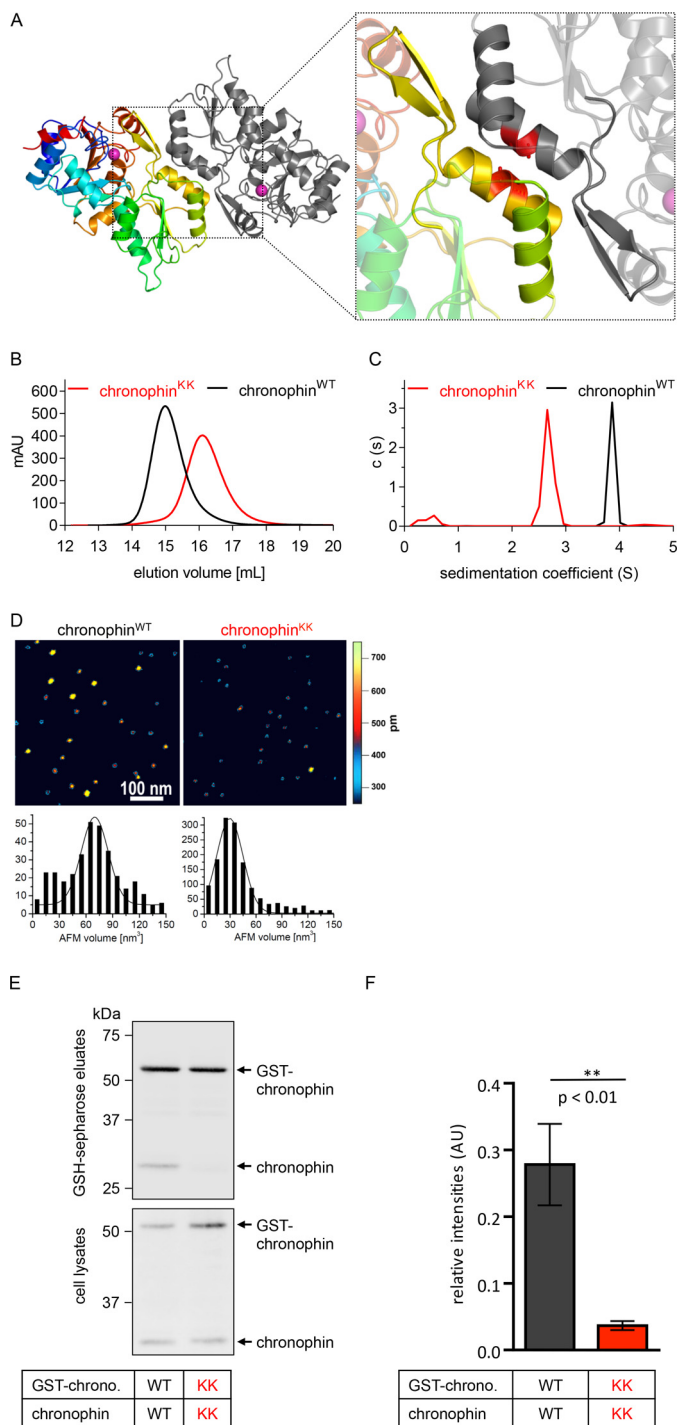
FIGURE 1. **Characterization of chronophin$^{KK}$.** A, ribbon diagram of the dimeric murine chronophin structure (Protein Data Bank code 4BX3). One protomer is shown in rainbow colors from the N terminus (*blue*) to the C terminus (*red*); the other protomer is represented in *gray*. The cofactor Mg$^{2+}$ (*magenta*-colored *sphere*) indicates the active site; the catalytic domain is shown in *blue/cyan* and *orange/red*. Dimerization is mediated by the capping domain (*green/yellow*). The *enlarged area* highlights helices $\alpha$6 (*green*)/$\alpha$7 (*yellow*) and the substrate specificity loop (*yellow*) that form the dimerization interface of chronophin. Ala$^{194}$ and Ala$^{195}$ in helix $\alpha$7 that are mutated to lysines in chronophin$^{KK}$ are depicted as *red sticks* in both monomers. B, analytical size exclusion chromatography shows a peak elution volume of chronophin$^{WT}$ (theoretical molecular mass, 31.8 kDa) at 14.9 ml, corresponding to a calculated molecular mass of 60.7 kDa. Chronophin$^{KK}$ is detected at a peak elution volume of 16.1 ml, corresponding to a calculated molecular mass of 33.7 kDa. C, analytical ultracentrifugation data demonstrate different sedimentation coefficients for chronophin$^{WT}$ and chronophin$^{KK}$ that correspond

nophin in Fig. 1*A* (see also Ref. 9). The cap consists of five central parallel $\beta$-strands that are connected by helices, and dimerization is mainly mediated by helix $\alpha$6 following $\beta$-strand 3, by a $\beta$-hairpin (referred to as substrate specificity loop) inserted after $\beta$-strand 4, and by the ensuing helix $\alpha$7. This substrate specificity loop also acts as a roof for the entrance to the active site.

*Creation of a Monomeric Murine Chronophin Variant*—To study the functional relevance of chronophin homodimerization, we exchanged the short, uncharged side chains of Ala$^{194}$ and Ala$^{195}$ in the murine chronophin dimerization interface (see Fig. 1*A*, *inset*) for the longer and charged side chains of Lys (chronophin$^{KK}$) and compared the oligomeric states of recombinantly expressed, purified chronophin$^{WT}$ and chronophin$^{KK}$ by size exclusion chromatography. Fig. 1*B* shows that chronophin (molecular mass, 31.8 kDa) has a peak elution volume that corresponds to a calculated molecular mass of 60.7 kDa, indicating that the protein indeed forms a stable dimer in solution. In contrast, chronophin$^{KK}$ has a peak elution volume corresponding to a calculated molecular mass of 33.7 kDa, equivalent to chronophin in a monomeric state. Analytical ultracentrifugation sedimentation velocity experiments confirmed a monomeric molecular mass for chronophin$^{KK}$ ($\sim$32 kDa), whereas wild type chronophin showed a sedimentation behavior consistent with a dimeric state ($\sim$56 kDa) (Fig. 1*C*). Furthermore, in AFM imaging experiments, chronophin$^{KK}$ showed protein volumes than are consistent with a monomeric state of this variant (30 $\pm$ 13 kDa for chronophin$^{KK}$ compared with 63 $\pm$ 18 kDa for chronophin$^{WT}$) (Fig. 1*D*).

To determine the oligomeric states of chronophin$^{WT}$ and chronophin$^{KK}$ in mammalian cells, we simultaneously expressed GST-tagged or untagged versions of chronophin$^{WT}$ and chronophin$^{KK}$ in HEK293 cells, performed pulldown binding experiments with glutathione-Sepharose beads, and subsequently probed bead-associated chronophin by Western blotting. The expectation is that GST-chronophin$^{WT}$ will pull down untagged chronophin$^{WT}$, whereas the monomerized chronophin$^{KK}$ will prevent co-precipitation. Fig. 1*E* demonstrates that GST-chronophin$^{WT}$ (detectable at $\sim$60 kDa after separation of the bead eluates by SDS-PAGE and immunoblotting with $\alpha$-chronophin antibodies) indeed associated with

to molecular masses of $\sim$56 and $\sim$32 kDa, respectively. D, atomic force microscopy images of chronophin$^{WT}$ and chronophin$^{KK}$. *Top*, images are 500 $\times$ 500 nm with a height scale of 0.75 nm. *Bottom*, Gaussian fits to statistical volume distributions for chronophin$^{WT}$ and chronophin$^{KK}$ give maxima of 70 nm$^3$ (337 particles) and 30 nm$^3$ (1,409 particles), respectively, which translate into a molecular masses of 63 and 30 kDa, respectively. A fraction of chronophin$^{WT}$ also shows protein volumes consistent with a monomeric state. E, GST pulldown experiments. GST-tagged chronophin$^{WT}$/chronophin$^{KK}$ (*GST-chrono. WT/GST-chrono. KK*) and untagged chronophin$^{WT}$/chronophin$^{KK}$ (*chronophin WT/chronophin KK*) were co-expressed in HEK293-AD cells as indicated. GST-chronophin was precipitated with glutathione-Sepharose beads, bead-associated proteins were separated by SDS-PAGE, and chronophin was detected with a chronophin-specific antibody by immunoblotting. Western blots of the corresponding whole cell lysates are shown to assess protein expression levels in cells. F, densitometric quantification of Western blots. The band corresponding to untagged chronophin was normalized to the GST-chronophin signal in each lane and compared with the optical density of the signal corresponding to chronophin$^{WT}$ precipitated with GST-chronophin$^{WT}$. The mean values $\pm$S.E. (*error bars*) of the relative intensities are shown ($n = 4$). *mAU*, milliabsorbance units; *AU*, absorbance units.
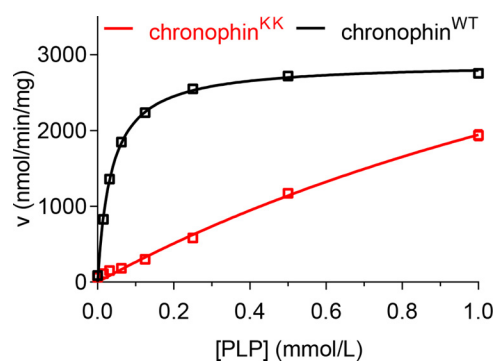
FIGURE 2. **Analysis of chronophin^KK phosphatase activity.** *In vitro* PLP phosphatase assays were performed in 96-well microtiter plates in a total assay volume of 50 $\mu$l using recombinantly expressed, purified chronophin^WT or chronophin^KK (0.16 $\mu$g of protein/well) and 0–1 mM PLP. The reaction was stopped with malachite green, and released inorganic phosphate was determined by measuring $A_{620}$. The enzyme velocities (*v*) toward increasing PLP concentrations are shown. Results represent mean values $\pm$ S.E. of three independent experiments performed with three independently purified batches of proteins. Note that most *error bars* are masked by the *symbols*.

**TABLE 3**

**Kinetic constants of chronophin^WT and chronophin^KK toward PLP**

PLP dephosphorylation was measured in 96-well microtiter plates in a total assay volume of 50 $\mu$l using recombinantly expressed, purified chronophin^WT or chronophin^KK (0.16 $\mu$g of protein/well) and 0–1 mM PLP. The reaction was stopped with malachite green, and released inorganic phosphate was determined by measuring $A_{620}$. The data are mean values $\pm$ S.E. of three independent experiments performed with three independently purified batches of proteins. $K_m$, Michaelis-Menten constant; $k_{cat}$, turnover number; $k_{cat}/K_m$, specificity constant. The $k_{cat}$ values were calculated from the maximum enzyme velocities using a molecular mass of 31.828 kDa for chronophin^WT and 31.942 kDa for chronophin^KK.

| | Chronophin^WT | Chronophin^KK |
|---|---|---|
| $K_m$ ($\mu$M) | 36 $\pm$ 1.2 | 2,387 $\pm$ 492 |
| $k_{cat}$ (s$^{-1}$) | 1.5 $\pm$ 0.01 | 3.5 $\pm$ 0.6 |
| $k_{cat}/K_m$ (s$^{-1}\cdot$M$^{-1}$) | 4.3 $\times$ 10$^4$ | 0.2 $\times$ 10$^4$ |

chronophin^WT (detectable at ~32 kDa) in pulldown binding assays, whereas an interaction of GST-chronophin^KK with chronophin^KK was not detectable. The results of four independent experiments are quantified in Fig. 1*F*. Together, these data clearly show that chronophin^KK is a monomer both *in vitro* and in mammalian cells.

*Enzymatic Properties of Monomeric Chronophin*—We next investigated the effect of chronophin monomerization on its enzymatic activity toward PLP. Fig. 2 demonstrates that whereas homodimeric chronophin efficiently dephosphorylates PLP the activity of the monomeric chronophin^KK variant is strongly impaired. This is mainly due to a ~65-fold increase in $K_m$, whereas the calculated $V_{max}$ remains largely unaffected. As a result, the catalytic efficiency ($k_{cat}/K_m$) of chronophin^KK is reduced to ~3.5% compared with chronophin^WT. The catalytic constants of chronophin^WT and chronophin^KK toward PLP are summarized in Table 3.

*Isothermal Titration Calorimetry of BeF$_3^-$ Binding to Chronophin^WT and Chronophin^KK*—To test whether the impaired catalytic efficiency of chronophin^KK is due to rearrangements in catalytic core residues, we measured the binding of chronophin to BeF$_3^-$. BeF$_3^-$ structurally mimics the phosphoaspartate transition state of HAD phosphatases by coordinating the catalytic core residues and the catalytically essential Mg$^{2+}$ as a phosphate analog (30–36). Fig. 3 shows that the interaction of BeF$_3^-$ with chronophin^WT and chronophin^KK can be optimally
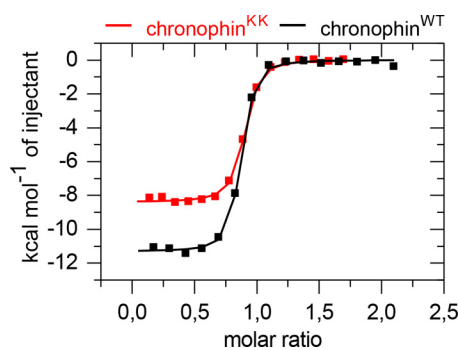


FIGURE 3. **Isothermal titration calorimetry-derived binding isotherms of BeF$_3^-$ titrated into chronophin^WT (■) or chronophin^KK (■).** Measured binding enthalpies are plotted as a function of the molar ratio of BeF$_3^-$ to the respective chronophin variant. Results are representative of three independent experiments performed with three independently purified batches of proteins.

**TABLE 4**

**Thermodynamic profiles of BeF$_3^-$ binding to chronophin^WT or chronophin^KK**

The data are mean values $\pm$ S.E. of three independent isothermal titration calorimetry experiments performed with three independently purified batches of proteins. $\Delta H$, enthalpy; T$\cdot\Delta S$, entropy; $N$, stoichiometry; $\Delta G$, Gibbs free energy; $K_d$, dissociation constant; ND, not determined.

| | Chronophin^WT | Chronophin^KK | *p* value |
|---|---|---|---|
| $\Delta H$ (kcal/mol) | $-11.92 \pm 0.33$ | $-8.72 \pm 0.20$ | 0.0011 |
| T$\cdot\Delta S$ (kcal/mol) | $-2.37 \pm 0.23$ | $0.23 \pm 0.18$ | 0.0009 |
| $N$ | $0.87 \pm 0.03$ | $0.84 \pm 0.01$ | ND |
| $\Delta G$ (kcal/mol) | $-9.55 \pm 0.20$ | $-8.95 \pm 0.02$ | 0.0034 |
| $K_d$ (nM) | $78 \pm 13$ | $215 \pm 7$ | 0.0008 |

fitted to a one-site binding model. The stoichiometry of BeF$_3^-$ binding is ~0.85 for chronophin^WT and chronophin^KK, indicating an equimolar interaction in both cases (Table 4). The apparent deviation from the 1:1 binding ratio is likely due to protein precipitation issues during the experiment. Thus, chronophin^WT and chronophin^KK bind BeF$_3^-$ with a comparable stoichiometry. Surprisingly, however, the BeF$_3^-$ binding constant of chronophin^KK is about 3-fold higher than that of chronophin^WT. Furthermore, the quantity of released heat ($\Delta H$), the entropic contribution ($\Delta S$) upon BeF$_3^-$ binding, and the resulting free Gibbs free energy ($\Delta G$) values also differ significantly between chronophin^WT and chronophin^KK (Table 4). Together, the *in vitro* phosphatase and ITC experiments suggest that the chronophin homodimer interface in the cap domain exerts allosteric effects on the catalytic cleft of the enzyme.

*Crystallization and Structure Determination of Chronophin^KK*— Therefore, we solved the structure of the monomerized chronophin variant. Chronophin^KK crystallized in the space group P2 and could be refined to 1.75-Å resolution with an $R_{work}$ of 19.1% and an $R_{free}$ of 23.6% (Protein Data Bank code 4BX0 and Table 2). The r.m.s.d. of 0.47 Å for the C$\alpha$ atoms of residues 1–290 between chronophin^WT and chronophin^KK clearly shows that the replacement of Ala$^{194}$ and Ala$^{195}$ with Lys residues in the cap domain had no impact on the overall fold of a chronophin protomer (Fig. 4*A*). However, the substrate specificity loop in chronophin^KK is tilted by ~25° compared with chronophin^WT (measured between the C$\alpha$ atoms of Asp$^{182}$ and Pro$^{187}$ of the respective molecules). The *enlarged areas* in Fig. 4*A* show that in chronophin^WT residues Trp$^{177}$ and Arg$^{185}$ in
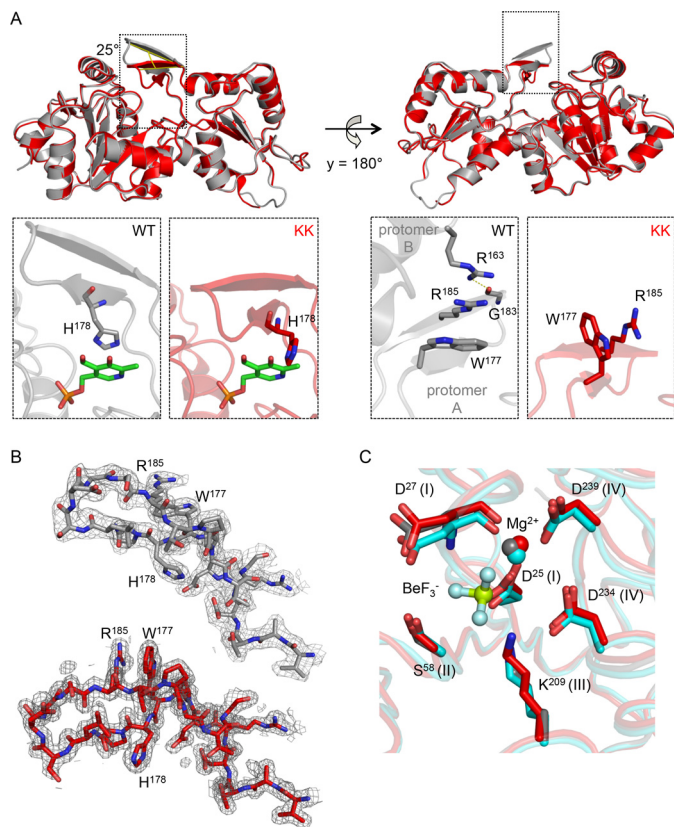
FIGURE 4. **Structural comparison of murine chronophin[WT] and chronophin[KK].** *A, upper left,* both structures are shown as ribbon diagrams and are superimposed. Chronophin[WT] (Protein Data Bank code 4BX3) is in *gray,* and chronophin[KK] (Protein Data Bank code 4BX0) is in *red.* The substrate specificity loop in chronophin[KK] is tilted by ~25° compared with chronophin[WT] as measured between the Cα atoms of Asp[182] and Pro[187] of the respective molecules. *Lower left panels,* detailed views show that in chronophin[WT] His[178] of the substrate specificity loop coordinates the pyridine ring of PLP by π-electron stacking. PLP has been introduced from Protein Data Bank code 2P69 for visualization purposes. The altered substrate specificity loop positioning in chronophin[KK] causes a reorientation of His[178] with its imidazole side chain now being almost perpendicular to the PLP pyridine ring. *Right panels,* back views of the structures. The detailed views in the *lower panels* reveal that in chronophin[WT] Trp[177] and Arg[185] in the substrate specificity loop of protomer A stack with Arg[163] of protomer B (which is not shown in the *upper panels*). Arg[163] additionally forms a hydrogen bond to the backbone carbonyl oxygen of Gly[183] in the substrate specificity loop of protomer A. These interprotomer interactions are absent in monomeric chronophin[KK]. *B,* electron density maps of residues 170–190. Shown are the refined $2F_o - F_c$ electron density maps contoured at an r.m.s.d. of 1 overlaid on the models of chronophin[WT] (*gray*) and chronophin[KK] (*red*). *C,* superposition of the active sites of chronophin[WT] (*gray;* Protein Data Bank code 4BX3) and chronophin[KK] (*red;* Protein Data Bank code 4BX0). Chronophin[WT] is additionally shown in the BeF$_3^-$-liganded state (*cyan;* Protein Data Bank code 4BX2). Catalytically essential residues of the HAD motifs I–IV (*roman numerals*) are indicated.

the substrate specificity loop (Pro[176]–Pro[187]) of protomer A stack together with Arg[163] of protomer B, which itself forms a hydrogen bond with the carbonyl oxygen atom in the backbone of Gly[183] in protomer A. Importantly, the imidazole ring of His[178] in the substrate specificity loop coordinates the pyridine ring of PLP by π-electron stacking (see Protein Data Bank code 2P69). In chronophin[KK], the interprotomer contacts are lost, resulting in a tilting of the substrate specificity loop and consequently an altered orientation of the substrate-binding His[178] residue (Fig. 4, *A* and *B*). These results demonstrate that contacts between the substrate specificity loop and the other protomer in the homodimer are crucial for the correct posi-

tioning of the substrate specificity loop and hence for the orientation of residues involved in substrate coordination.

To elucidate whether all catalytic core residues in monomeric chronophin are oriented correctly, we compared the HAD motif I–IV catalytic core residues of chronophin[KK] and chronophin[WT] with chronophin[WT] in complex with BeF$_3^-$. The chronophin[WT]-BeF$_3^-$ structure was refined to 2.2-Å resolution with an $R_{work}$ of 16.8% and an $R_{free}$ of 21.2% (Protein Data Bank code 4BX2; see Table 2 for data collection and refinement statistics). (Note that we were unable to crystallize chronophin[KK] in complex with BeF$_3^-$. Co-crystallization attempts failed due to protein precipitation issues, and soaking experiments resulted in broken crystals). Fig. 4*C* shows that the positioning of these amino acids does not differ substantially between chronophin[WT] and chronophin[KK] and further confirms that the cofactor Mg$^{2+}$ is properly coordinated. We conclude from these results that the impaired binding of BeF$_3^-$ to monomeric chronophin (see Fig. 3 and Table 3) is not due to conformational changes in the active site residues of chronophin[KK].

Together, the results of the steady-state enzyme kinetics, the ITC experiments, and the structural analyses support the conclusion that the core catalytic machinery of the monomeric chronophin[KK] variant is unaltered compared with homodimeric chronophin. However, the tilting of the substrate specificity loop and the subsequent reorientation of the PLP-binding His[178] residue in the cap domain of the monomer lead to a marked increase in the $K_m$ value toward the substrate PLP. The reduced binding affinity (albeit identical binding stoichiometry) of chronophin[KK] to BeF$_3^-$ compared with chronophin[WT] may thus indicate a diminished accessibility of the active site for BeF$_3^-$ due to the tilted substrate specificity loop.

*Potential General Role of Dimerization for the Function of C2-capped HAD Phosphatases*—Are the mode and function of chronophin dimerization for the positioning of the substrate specificity loop/β-hairpin a unique feature of this phosphatase or a characteristic trait of C2a-capped HAD hydrolases in general? We addressed this question by performing a DALI structure similarity search with human chronophin (Protein Data Bank code 2OYC) as a search model. The results were manually curated to select members of the C2a subfamily of HAD hydrolases. In accordance with the results shown in Table 1, we found 16 structures in addition to human chronophin and the newly solved structure of murine chronophin. The r.m.s.d. values for structural alignments of all Cα atoms of these family members with murine chronophin indicate high structural homology, although the amino acid sequence identities between these proteins and murine chronophin are very low (ranging from 16.1 to 28.3% with the exception of human chronophin that is 91.2% identical with murine chronophin). PDBePISA analysis indicates that all 18 molecules are highly likely to exist as homodimers as judged by the buried surface areas of ~1,000 Å$^2$ at the respective dimer interfaces. Five of them possibly form tetramers (dimers of dimers). The C2a-capped HAD hydrolases, r.m.s.d. values, and results of the PDBePISA analysis are listed in Table 5.

Fig. 5 shows the dimer interfaces of the structurally characterized homodimeric C2a-type HAD hydrolases identified in this analysis. All dimer interfaces are composed of two homol-

**TABLE 5**

**Oligomeric states of structurally characterized C2a-type HAD phosphatases**

r.m.s.d. values for structural alignments of all Cα atoms of family members with murine chronophin (Protein Data Bank code 4BX3) were calculated using PyMOL.

| UniProtKB (Protein Data Bank code) | Organism | r.m.s.d. compared with 4BX3 | Dimer interface ($\Delta^i G$)$^{a,b}$ |
|---|---|---|---|
| | | *Å* | *Å²* (*kcal/mol*) |
| Q96GD0 (2OYC) | *Homo sapiens* | 0.67 | 1,036 (−16.4) |
| P60487(4BX3) | *Mus musculus* | − | 992 (−14.7) |
| Q9H0R4 (3HLT) | *H. sapiens* | 2.47 | 1,315 (−13.9) |
| Q3UGR5 (2HO4) | *M. musculus* | 3.08 | 1,300 (−13.6) |
| Q9H008 (2X4D) | *H. sapiens* | 2.17 | 1,307 (−17.9) |
| P36151 (3RF6) | *S. cerevisiae* | 10.61 | 1,866 (−25.7) |
| O32125 (3PDW) | *Bacillus subtilis* | 2.69 | 1,203 (−15.3) |
| Q11S56 (2HX1) | *Cytophaga hutchinsonii* ATCC 33406 | 2.44 | 980 (−13.7) *1,273 (−5.2)* |
| Q836C7 (1YV9) | *Enterococcus faecalis* V583 | 1.66 | 1,151 (−12.2) |
| P0AF24 (2C4N) | *E. coli* K-12 | 2.02 | 1,097 (−23.8) *1,072 (−6.6)* |
| L7N4Y2 (4I9F) | *Mycobacterium tuberculosis* | 2.31 | 1,146 (−19.6) |
| O59622 (1ZJJ) | *Pyrococcus horikoshii* OT3 | 1.78 | 1,162 (−18.9) |
| Q8E044 (3EPR) | *Streptococcus agalactiae* | 1.69 | 1,143 (−12.9) *1,048 (−5.8)* |
| Q8DTD6 (1WVI) | *Streptococcus mutans* UA159 | 1.94 | 1,157 (−15.3) *955 (−4.3)* |
| Q97Q24 (1YDF) | *Streptococcus pneumoniae* | 2.13 | 1,080 (−12.7) |
| Q99ZW4 (1YS9) | *Streptococcus pyogenes* | 1.67 | 1,185 (−14.1) *868 (−4.8)* |
| Q9X264 (1VJR) | *Thermotoga maritima* | 1.91 | 1,033 (−14.7) |
| O29873 (3QGM) | *Archaeoglobus fulgidus* | 1.71 | 1,315 (−23.8) |

$^a$ Buried surface areas and $\Delta^i G$ were calculated using the PDBePISA online tool. $\Delta^i G$, solvation-free energy gain upon formation of the interface (not taking into account the effect of satisfied hydrogen bonds and salt bridges across the interface). Negative $\Delta^i G$ values correspond to hydrophobic interfaces or to positive protein affinity (23).

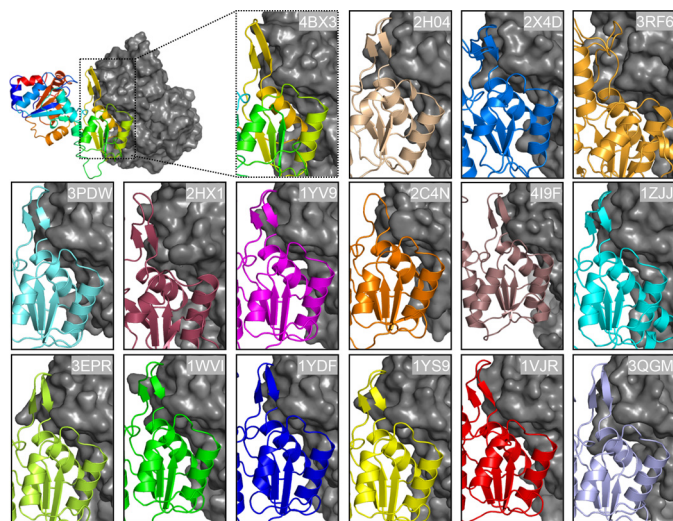$^b$ Values in italics correspond to potential tetramer interfaces.



**FIGURE 5. Homodimerization interfaces in C2a-type HAD hydrolases.** Protomer A is shown in a *colored* ribbon representation, whereas protomer B is shown in *gray* surface representation. Protein Data Bank codes are indicated. The structures of human pyridoxal 5′-phosphate phosphatase/chronophin (Protein Data Bank code 2OYC) and human HDHD2 (Protein Data Bank code 3HLT) are very similar to the murine orthologs (Protein Data Bank codes 3BX4 and 2HO4) and are therefore not shown. All dimer interfaces are composed of two homologous helices and contain a β-hairpin structure that resembles the substrate specificity loop in chronophin. Although hydrogen bonds are present in the loops of Protein Data Bank codes 2C4N and 3RF6, they are not shown as β-sheets by the automatic secondary structure assignment because the participating residues are not adjacent to each other in the sequence.

ogous α-helices in the cap domains and contain a β-hairpin structure that resembles the substrate specificity loop in chronophin. We note that although hydrogen bonds are present in the corresponding loop structure of the uncharacterized *Saccharomyces cerevisiae* protein YKR070W (Protein Data Bank code 3RF6) and the *Escherichia coli* protein NagD (Protein Data

Bank code 2C4N (7)), they are not shown as β-sheets by the automatic secondary structure assignment because the participating residues are not adjacent to each other in the sequence. Nevertheless, the corresponding loop structure also participates in interprotomer contacts and may likewise also contribute to substrate specificity. Therefore, dimerization appears to be a general prerequisite for the proper positioning of the β-hairpin substrate specificity loop (or of corresponding elements) in all C2a-capped HAD hydrolases structurally characterized to date.

## DISCUSSION

Substrate specificity in capped HAD phosphatases is accomplished by cap movements that facilitate active site solvent exclusion and by specificity determinants encoded in the cap domain. We identify homodimerization via C2a-type caps as a previously unrecognized factor involved in substrate specificity control. We demonstrate that the constitutive homodimerization of chronophin is a prerequisite for the proper positioning of the substrate specificity loop and consequently for efficient PLP dephosphorylation. Thus, the specificity of chronophin toward PLP as a substrate depends on an allosteric effect induced by a homophilic intermolecular interaction. Crystal structure analyses of oligomeric C2a-type HAD hydrolases from different species reveal that the positioning of the β-hairpin/presumable substrate specificity loop via homodimerization is a conserved and common feature in this structural subfamily. Our results therefore suggest a general principle of how the dimerization of C2a-capped HAD hydrolases can contribute to substrate specificity.

Although the role of homodimerization in the C2a family has not been investigated so far, the relevance of oligomerization for C1- and C0-type HAD hydrolase functions was addressed in previous studies. For example, homodimerization of the

## Role of Chronophin Dimerization

C1-type *Haemophilus influenzae* P4 acid phosphatase is important for catalysis because side chains of one protomer stabilize the conformation of catalytic loop IV in the active site of the other protomer. Such intersubunit contacts that reach into the catalytic site may also be important for substrate recognition (37). The C1-capped mammalian cytosolic 5′-nucleotidase (cN-II) exists as a tetramer in its native form. Although a dimeric mutant of this protein is still active, monomeric cN-II is inactive, suggesting that enzymatic activity may be controlled by switching the oligomeric state, although the underlying mechanism is unknown (38, 39). Structural analysis of the tetrameric, C0-type (capless) HAD phosphatase KdsC from *E. coli* has revealed that protomers can act as cap surrogates to shield the active site of an adjacent protomer and to supply residues involved in substrate recognition (40). A similar tetrameric organization was reported for the *Bacteroides thetaiotaomicron* KDN-9-P phosphatase (41). Homooligomeric interfaces may also contribute to proper folding or stability of the active site as has been proposed for the bifunctional C0-type T4 polynucleotide kinase/phosphatase PNKP (42). Taken together, the constitutive dimer formation of oligomeric HAD phosphatases appears to be generally required for appropriate catalytic activity and can also contribute to substrate coordination. Our finding that homodimerization is necessary for the proper orientation of the β-hairpin/substrate specificity loop in the C2a-capped HAD phosphatase chronophin further advances our mechanistic understanding of HAD phosphatase specificity control.

Self-association of proteins to form dimers or higher order oligomers is frequently observed (43). Oligomerization provides a simple way to increase protein complexity and can result in structural (*e.g.* improved stability) and functional advantages (*e.g.* control over active site accessibility and specificity) (44). In some oligomeric proteins, protomers must be stably assembled to build a functional protein; this may be the case for the constitutively oligomeric HAD phosphatases characterized to date. Some "classical," non-HAD-type phosphatases such as *E. coli* alkaline phosphatase are also known to form obligate homodimers and to lose structural stability and catalytic activity upon monomerization (45). In other homooligomeric proteins, the association and dissociation of protomers is reversible and can serve as a (concentration-sensing) mechanism to regulate enzyme activity (43, 46–48). Some receptor-like protein-tyrosine phosphatases utilize this mechanism of dynamic regulation. For example, protein-tyrosine phosphatase α, CD45, and SAP-1 are reversibly inhibited by dimer formation, which can be controlled by ligand binding (49), phosphorylation (50), or oxidative stress (51). Here, dimerization leads to a reciprocal occlusion of the catalytic site of each phosphatase protomer (52, 53). It is currently unknown whether those HAD phosphatases that are assigned as monomeric can associate to form homo- or heterooligomers in a stimulus-dependent manner in cells. Conversely, it is unclear whether oligomeric C2a-type HAD hydrolases such as chronophin can also be present in a monomeric form *in vivo*, for example below a threshold concentration, in particular subcellular compartments, or upon posttranslational modification.

## REFERENCES

1. Allen, K. N., and Dunaway-Mariano, D. (2009) Markers of fitness in a successful enzyme superfamily. *Curr. Opin. Struct. Biol.* **19,** 658–665
2. Aravind, L., and Koonin, E. V. (1998) The HD domain defines a new superfamily of metal-dependent phosphohydrolases. *Trends Biochem. Sci.* **23,** 469–472
3. Burroughs, A. M., Allen, K. N., Dunaway-Mariano, D., and Aravind, L. (2006) Evolutionary genomics of the HAD superfamily: understanding the structural adaptations and catalytic diversity in a superfamily of phosphoesterases and allied enzymes. *J. Mol. Biol.* **361,** 1003–1034
4. Seifried, A., Schultz, J., and Gohla, A. (2013) Human HAD phosphatases: structure, mechanism, and roles in health and disease. *FEBS J.* **280,** 549–571
5. Lahiri, S. D., Zhang, G., Dunaway-Mariano, D., and Allen, K. N. (2006) Diversification of function in the haloacid dehalogenase enzyme superfamily: the role of the cap domain in hydrolytic phosphoruscarbon bond cleavage. *Bioorg. Chem.* **34,** 394–409
6. Lu, Z., Dunaway-Mariano, D., and Allen, K. N. (2005) HAD superfamily phosphotransferase substrate diversification: structure and function analysis of HAD subclass IIB sugar phosphatase BT4131. *Biochemistry* **44,** 8684–8696
7. Tremblay, L. W., Dunaway-Mariano, D., and Allen, K. N. (2006) Structure and activity analyses of *Escherichia coli* K-12 NagD provide insight into the evolution of biochemical function in the haloalkanoic acid dehalogenase superfamily. *Biochemistry* **45,** 1183–1193
8. Walldén, K., Rinaldo-Matthis, A., Ruzzenente, B., Rampazzo, C., Bianchi, V., and Nordlund, P. (2007) Crystal structures of human and murine deoxyribonucleotidases: insights into recognition of substrates and nucleotide analogues. *Biochemistry* **46,** 13809–13818
9. Almo, S. C., Bonanno, J. B., Sauder, J. M., Emtage, S., Dilorenzo, T. P., Malashkevich, V., Wasserman, S. R., Swaminathan, S., Eswaramoorthy, S., Agarwal, R., Kumaran, D., Madegowda, M., Ragumani, S., Patskovsky, Y., Alvarado, J., Ramagopal, U. A., Faber-Barata, J., Chance, M. R., Sali, A., Fiser, A., Zhang, Z. Y., Lawrence, D. S., and Burley, S. K. (2007) Structural genomics of protein phosphatases. *J. Struct. Funct. Genomics* **8,** 121–140
10. Fonda, M. L. (1992) Purification and characterization of vitamin B$_6$-phosphate phosphatase from human erythrocytes. *J. Biol. Chem.* **267,** 15978–15983
11. Jang, Y. M., Kim, D. W., Kang, T. C., Won, M. H., Baek, N. I., Moon, B. J., Choi, S. Y., and Kwon, O. S. (2003) Human pyridoxal phosphatase. Molecular cloning, functional expression, and tissue distribution. *J. Biol. Chem.* **278,** 50040–50046
12. Gohla, A., Birkenfeld, J., and Bokoch, G. M. (2005) Chronophin, a novel HAD-type serine protein phosphatase, regulates cofilin-dependent actin dynamics. *Nat. Cell Biol.* **7,** 21–29
13. Zoudilova, M., Kumar, P., Ge, L., Wang, P., Bokoch, G. M., and DeFea, K. A. (2007) β-Arrestin-dependent regulation of the cofilin pathway downstream of protease-activated receptor-2. *J. Biol. Chem.* **282,** 20634–20646
14. Sun, C. X., Magalhães, M. A., and Glogauer, M. (2007) Rac1 and Rac2 differentially regulate actin free barbed end formation downstream of the fMLP receptor. *J. Cell Biol.* **179,** 239–245
15. Huang, T. Y., Minamide, L. S., Bamburg, J. R., and Bokoch, G. M. (2008) Chronophin mediates an ATP-sensing mechanism for cofilin dephosphorylation and neuronal cofilin-actin rod formation. *Dev. Cell* **15,** 691–703
16. Ivanovska, J., Tregubova, A., Mahadevan, V., Chakilam, S., Gandesiri, M., Benderska, N., Ettle, B., Hartmann, A., Söder, S., Ziesché, E., Fischer, T., Lautscham, L., Fabry, B., Segerer, G., Gohla, A., and Schneider-Stock, R. (2013) Identification of DAPK as a scaffold protein for the LIMK/cofilin complex in TNF-induced apoptosis. *Int. J. Biochem. Cell Biol.* **45,** 1720–1729
17. Li, C., Liang, Y. Y., Feng, X. H., Tsai, S. Y., Tsai, M. J., and O'Malley, B. W. (2008) Essential phosphatases and a phospho-degron are critical for reg-

ulation of SRC-3/AIB1 coactivator function and turnover. *Mol. Cell* **31,** 835–849

18. Bowling, F. G. (2011) Pyridoxine supply in human development. *Semin. Cell Dev. Biol.* **22,** 611–618

19. di Salvo, M. L., Safo, M. K., and Contestabile, R. (2012) Biomedical aspects of pyridoxal 5′-phosphate availability. *Front. Biosci.* **4,** 897–913

20. Kim, J. E., Kim, D. W., Kwak, S. E., Kwon, O. S., Choi, S. Y., and Kang, T. C. (2008) Potential role of pyridoxal-5′-phosphate phosphatase/chronopin in epilepsy. *Exp. Neurol.* **211,** 128–140

21. Kim, J. E., Ryu, H. J., Kim, M. J., Kim, D. W., Kwon, O. S., Choi, S. Y., and Kang, T. C. (2010) Pyridoxal-5′-phosphate phosphatase/chronophin induces astroglial apoptosis via actin-depolymerizing factor/cofilin system in the rat brain following status epilepticus. *Glia* **58,** 1937–1948

22. Pandya, C., Brown, S., Pieper, U., Sali, A., Dunaway-Mariano, D., Babbitt, P. C., Xia, Y., and Allen, K. N. (2013) Consequences of domain insertion on sequence-structure divergence in a superfold. *Proc. Natl. Acad. Sci. U.S.A.* **110,** E3381–E3387

23. Krissinel, E., and Henrick, K. (2007) Inference of macromolecular assemblies from crystalline state. *J. Mol. Biol.* **372,** 774–797

24. Schuck, P. (2000) Size-distribution analysis of macromolecules by sedimentation velocity ultracentrifugation and Lamm equation modeling. *Biophys. J.* **78,** 1606–1619

25. Roth, H. M., Römer, J., Grundler, V., Van Houten, B., Kisker, C., and Tessmer, I. (2012) XPB helicase regulates DNA incision by the *Thermoplasma acidophilum* endonuclease Bax1. *DNA Repair* **11,** 286–293

26. Battye, T. G., Kontogiannis, L., Johnson, O., Powell, H. R., and Leslie, A. G. (2011) iMOSFLM: a new graphical interface for diffraction-image processing with MOSFLM. *Acta Crystallogr. D Biol. Crystallogr.* **67,** 271–281

27. Evans, P. (2006) Scaling and assessment of data quality. *Acta Crystallogr. D Biol. Crystallogr.* **62,** 72–82

28. McCoy, A. J., Grosse-Kunstleve, R. W., Adams, P. D., Winn, M. D., Storoni, L. C., and Read, R. J. (2007) Phaser crystallographic software. *J. Appl. Crystallogr.* **40,** 658–674

29. Afonine, P. V., Grosse-Kunstleve, R. W., Adams, P. D., Lunin, V. Y., and Urzhumtsev, A. (2007) On macromolecular refinement at subatomic resolution with interatomic scatterers. *Acta Crystallogr. D Biol. Crystallogr.* **63,** 1194–1197

30. Cho, H., Wang, W., Kim, R., Yokota, H., Damo, S., Kim, S. H., Wemmer, D., Kustu, S., and Yan, D. (2001) $BeF_3^-$ acts as a phosphate analog in proteins phosphorylated on aspartate: structure of a $BeF_3^-$ complex with phosphoserine phosphatase. *Proc. Natl. Acad. Sci. U.S.A* **98,** 8525–8530

31. Roberts, A., Lee, S. Y., McCullagh, E., Silversmith, R. E., and Wemmer, D. E. (2005) YbiV from *Escherichia coli* K12 is a HAD phosphatase. *Proteins* **58,** 790–801

32. Wang, W., Cho, H. S., Kim, R., Jancarik, J., Yokota, H., Nguyen, H. H., Grigoriev, I. V., Wemmer, D. E., and Kim, S. H. (2002) Structural characterization of the reaction pathway in phosphoserine phosphatase: crystallographic "snapshots" of intermediate states. *J. Mol. Biol.* **319,** 421–431

33. Rinaldo-Matthis, A., Rampazzo, C., Reichard, P., Bianchi, V., and Nordlund, P. (2002) Crystal structure of a human mitochondrial deoxyribonucleotidase. *Nat. Struct. Biol.* **9,** 779–787

34. Jung, S. K., Jeong, D. G., Chung, S. J., Kim, J. H., Park, B. C., Tonks, N. K., Ryu, S. E., and Kim, S. J. (2010) Crystal structure of ED-Eya2: insight into dual roles as a protein tyrosine phosphatase and a transcription factor. *FASEB J.* **24,** 560–569

35. Ghosh, A., Shuman, S., and Lima, C. D. (2008) The structure of Fcp1, an essential RNA polymerase II CTD phosphatase. *Mol. Cell* **32,** 478–490

36. Kim, Y., Gentry, M. S., Harris, T. E., Wiley, S. E., Lawrence, J. C., Jr., and Dixon, J. E. (2007) A conserved phosphatase cascade that regulates nuclear membrane biogenesis. *Proc. Natl. Acad. Sci. U.S.A* **104,** 6596–6601

37. Felts, R. L., Ou, Z., Reilly, T. J., and Tanner, J. J. (2007) Structure of recombinant *Haemophilus influenzae* e (P4) acid phosphatase reveals a new member of the haloacid dehalogenase superfamily. *Biochemistry* **46,** 11110–11119

38. Spychala, J., Chen, V., Oka, J., and Mitchell, B. S. (1999) ATP and phosphate reciprocally affect subunit association of human recombinant High Km 5′-nucleotidase. Role for the C-terminal polyglutamic acid tract in subunit association and catalytic activity. *Eur. J. Biochem.* **259,** 851–858

39. Pesi, R., Allegrini, S., Careddu, M. G., Filoni, D. N., Camici, M., and Tozzi, M. G. (2010) Active and regulatory sites of cytosolic 5′-nucleotidase. *FEBS J.* **277,** 4863–4872

40. Biswas, T., Yi, L., Aggarwal, P., Wu, J., Rubin, J. R., Stuckey, J. A., Woodard, R. W., and Tsodikov, O. V. (2009) The tail of KdsC: conformational changes control the activity of a haloacid dehalogenase superfamily phosphatase. *J. Biol. Chem.* **284,** 30594–30603

41. Lu, Z., Wang, L., Dunaway-Mariano, D., and Allen, K. N. (2009) Structure-function analysis of 2-keto-3-deoxy-D-glycero-D-galactononononate-9-phosphate phosphatase defines specificity elements in type C0 haloalkanoate dehalogenase family members. *J. Biol. Chem.* **284,** 1224–1233

42. Zhu, H., Smith, P., Wang, L. K., and Shuman, S. (2007) Structure-function analysis of the 3′ phosphatase component of T4 polynucleotide kinase/phosphatase. *Virology* **366,** 126–136

43. Marianayagam, N. J., Sunde, M., and Matthews, J. M. (2004) The power of two: protein dimerization in biology. *Trends Biochem. Sci.* **29,** 618–625

44. Neet, K. E., and Timm, D. E. (1994) Conformational stability of dimeric proteins: quantitative studies by equilibrium denaturation. *Protein Sci.* **3,** 2167–2174

45. Boulanger, R. R., Jr., and Kantrowitz, E. R. (2003) Characterization of a monomeric *Escherichia coli* alkaline phosphatase formed upon a single amino acid substitution. *J. Biol. Chem.* **278,** 23497–23501

46. Hashimoto, K., Nishi, H., Bryant, S., and Panchenko, A. R. (2011) Caught in self-interaction: evolutionary and functional mechanisms of protein homooligomerization. *Phys. Biol.* **8,** 035007

47. Mei, G., Di Venere, A., Rosato, N., and Finazzi-Agrò, A. (2005) The importance of being dimeric. *FEBS J.* **272,** 16–27

48. Mazurek, S. (2011) Pyruvate kinase type M2: a key regulator of the metabolic budget system in tumor cells. *Int. J. Biochem. Cell Biol.* **43,** 969–980

49. Tonks, N. K. (2006) Protein tyrosine phosphatases: from genes, to function, to disease. *Nat. Rev. Mol. Cell Biol.* **7,** 833–846

50. Bilwes, A. M., den Hertog, J., Hunter, T., and Noel, J. P. (1996) Structural basis for inhibition of receptor protein-tyrosine phosphatase-α by dimerization. *Nature* **382,** 555–559

51. van der Wijk, T., Blanchetot, C., Overvoorde, J., and den Hertog, J. (2003) Redox-regulated rotational coupling of receptor protein-tyrosine phosphatase α dimers. *J. Biol. Chem.* **278,** 13968–13974

52. Chin, C. N., Sachs, J. N., and Engelman, D. M. (2005) Transmembrane homodimerization of receptor-like protein tyrosine phosphatases. *FEBS Lett.* **579,** 3855–3858

53. Wälchli, S., Espanel, X., and Hooft van Huijsduijnen, R. (2005) Sap-1/PTPRH activity is regulated by reversible dimerization. *Biochem. Biophys. Res. Commun.* **331,** 497–502

54. Chen, V. B., Arendall, W. B., 3rd, Headd, J. J., Keedy, D. A., Immormino, R. M., Kapral, G. J., Murray, L. W., Richardson, J. S., and Richardson, D. C. (2010) MolProbity: all-atom structure validation for macromolecular crystallography. *Acta Crystallogr. D Biol. Crystallogr.* **66,** 12–21